EUMETSAT Satellite Application Facility on Climate Monitoring

The EUMETSAT
Network of
Satellite
Application
Facilities

CM SAF

Climate Monitoring

Algorithm Theoretical Basis Document
SEVIRI Cloud Physical Products
CLAAS Edition 2

Document Signature Table

	Name	Function	Signature	Date
Author	Jan Fokke Meirink Gerd-Jan van Zadelhoff	CM SAF scientist CM SAF scientist		28/04/2015
Editor	Rainer Hollmann	Science Coordinator		10/06/2016
Approval	Rainer Hollmann	Science Coordinator		10/06/2016
Release	Martin Werscheck	SAF Manager		

Distribution List

Internal Distribution	
Name	**No. Copies**
DWD Archive	1
CM SAF Team	1

External Distribution		
Company	**Name**	**No. Copies**
PUBLIC		

Document Change Record

Issue/ Revision	Date	DCN No.	Changed Pages/Paragraphs
1.0	02/10/2012	SAF/CM/KNMI/ATBD/SEVIRI/CPP_1.0	Initial release prepared for DRI7
1.1	14/02/2013	SAF/CM/KNMI/ATBD/SEVIRI/CPP_1.1	Revised version following DRI RIDs
2.0	28/04/2015	SAF/CM/KNMI/ATBD/SEVIRI/CPP_2.0	Initial release for CLAAS edition 2 PCR
2.1	21/07/2015	SAF/CM/KNMI/ATBD/SEVIRI/CPP_2.1	Revised version following PCR RIDs
2.2	10/06/2016	SAF/CM/KNMI/ATBD/SEVIRI/CPP_2.2	Revised version following DRR 2.4 RIDs;

	Algorithm Theoretical Basis Document SEVIRI Cloud Physical Products CLAAS Edition 2	Doc. No.: SAF/CM/KNMI/ATBD/SEVIRI/CPP Issue: 2.2 Date: 10.06.2016

Table of Contents

List of figures

List of tables

Applicable documents

Reference	Title	Code
AD-1	EUMETSAT CM SAF CDOP 2 Product Requirements Document (PRD)	SAF/CM/DWD/PRD/2.7

Reference documents

Reference	Title	Code
RD-1	Algorithm Theoretical Basis Document SAFNWC/MSG "Cloud Products" (CMa-PGE01 v3.2, CT-PGE02 v2.2 & CTTH-PGE03 v2.2)	SAF/NWC/CDOP/MFL/SCI/ATBD/01, Issue 3, Rev. 2, 15/02/2012
RD-2	Algorithm Theoretical Basis Document: SEVIRI cloud products, CLAAS Edition 2	SAF/CM/DWD/ATBD/SEV/CLD, v2.3
RD-3	RTTOV v11 Users Guide	NWPSAF-MO-UD-028, Version 1.3, 13/06/2014

1. The EUMETSAT SAF on Climate Monitoring

The importance of climate monitoring with satellites was recognized in 2000 by EUMETSAT Member States when they amended the EUMETSAT Convention to affirm that the EUMETSAT mandate is also to "contribute to the operational monitoring of the climate and the detection of global climatic changes". Following this, EUMETSAT established within its Satellite Application Facility (SAF) network a dedicated centre, the SAF on Climate Monitoring (CM SAF, http://www.cmsaf.eu).

The consortium of CM SAF currently comprises the Deutscher Wetterdienst (DWD) as host institute, and the partners from the Royal Meteorological Institute of Belgium (RMIB), the Finnish Meteorological Institute (FMI), the Royal Meteorological Institute of the Netherlands (KNMI), the Swedish Meteorological and Hydrological Institute (SMHI), the Meteorological Service of Switzerland (MeteoSwiss), and the Meteorological Service of the United Kingdom (UK MetOffice). Since the beginning in 1999, the EUMETSAT Satellite Application Facility on Climate Monitoring (CM SAF) has developed and will continue to develop capabilities for a sustained generation and provision of Climate Data Records (CDR's) derived from operational meteorological satellites.

In particular, the generation of long-term data records is pursued. The ultimate aim is to make the resulting data records suitable for the analysis of climate variability and potentially the detection of climate trends. CM SAF works in close collaboration with the EUMETSAT Secretariat and liaises with other satellite operators to advance the availability, quality and usability of Fundamental Climate Data Records (FCDRs) as defined by the Global Climate Observing System (GCOS). As a major task the CM SAF utilizes FCDRs to produce records of Essential Climate Variables (ECVs) as defined by GCOS. Thematically, the focus of CM SAF is on ECVs associated with the global energy and water cycle.

Another essential task of CM SAF is to produce data records that can serve applications related to the Global Framework of Climate Services initiated by the WMO World Climate Conference-3 in 2009. CM SAF is supporting climate services at national meteorological and hydrological services (NMHSs) with long-term data records but also with data records produced close to real time that can be used to prepare monthly/annual updates of the state of the climate. Both types of products together allow for a consistent description of mean values, anomalies, variability and potential trends for the chosen ECVs. CM SAF ECV data records also serve the improvement of climate models both at global and regional scale.

As an essential partner in the related international frameworks, in particular WMO SCOPE-CM (Sustained COordinated Processing of Environmental satellite data for Climate Monitoring), the CM SAF - together with the EUMETSAT secretariat, assumes the role as main implementer of EUMETSAT's commitments in support to global climate monitoring. This is achieved through:

- Application of highest standards and guidelines as lined out by GCOS for the satellite data processing,

- Processing of satellite data within a true international collaboration benefiting from developments at international level and pollinating the partnership with own ideas and standards,

- Intensive validation and improvement of the CM SAF climate data records,

- Taking a major role in data record assessments performed by research organisations such as WCRP (World Climate Research Program). This role provides the CM SAF

with deep contacts to research organizations that form a substantial user group for the CM SAF CDRs,

- Maintaining and providing an operational and sustained infrastructure that can serve the community within the transition of mature CDR products from the research community into operational environments.

A catalogue of all available CM SAF products is accessible via the CM SAF webpage, http:/www.cmsaf.eu/. Here, detailed information about product ordering, add-on tools, sample programs and documentation is provided.

2. Introduction

This CM SAF Algorithm Theoretical Basis Document (ATBD) provides detailed information on the retrieval algorithms that are used to derive a data record of cloud physical products (CPP) from MSG-SEVIRI measurements. Disseminated products are instantaneous, daily and monthly cloud thermodynamic phase (CPH), liquid water path (LWP) and ice water path (IWP). The LWP and IWP products contain as additional layers the cloud optical thickness and particle effective radius. Table 1 shows the corresponding product numbers.

Table 1: Overview of CM SAF products covered in this ATBD.

Product	Product number
CPH	CM-21041
LWP	CM-21051
IWP	CM-21061

The algorithm description in this document is largely based on Roebeling (2008). The CPP algorithm and products have been used for many studies (e.g., Roebeling et al. 2006, 2008; Wolters et al. 2008; Roebeling and Van Meijgaard 2009; Greuell and Roebeling 2009; Wolters et al. 2010; Greuell et al. 2011).

The cloud physical properties retrieval algorithms are run for cloudy pixels only. The selection of cloudy pixels is done on the basis of the NWC-SAF cloud mask, also used in the CM SAF for the determination of cloud fraction (RD-1).

In Section 3 an overview of the retrieval algorithms is presented. Section 4 gives a detailed description of the retrieval algorithms, consisting of the relevant underlying physics (Section 4.1), the radiative transfer modelling (Section 4.2), the implementation of the retrieval scheme (Section 4.3), the error budget of the retrieved products (Section 4.4), and the practical application of the algorithms (Section 4.5). Finally, assumptions and limitations are discussed in Section 5.

3. Algorithm Overview

The CPP (cloud physical properties) algorithm version 5.2 consists of two main parts. First, the cloud phase (CPH), representing the thermodynamic phase of particles near the top of the cloud, is determined from a cloud typing approach developed by NOAA's Clouds from AVHRR Extended (CLAVR-x) team. This cloud type algorithm consists of a series of threshold tests applied to observed and simulated infrared brightness temperatures.

The algorithm then proceeds with retrieving cloud optical thickness (COT or τ) and cloud particle effective radius (REF or re), as well as liquid/ice water path (LWP/IWP), during daytime given the thermodynamic phase determined before (which is then assumed to be valid over the full vertical extension of the cloud). This retrieval scheme was developed at KNMI, and first described in Roebeling et al. (2006). The algorithm works via iteratively matching observed reflectances in two shortwave channels to simulated reflectances. It is based on earlier methods that retrieve cloud optical thickness and cloud particle effective radius from satellite radiances at wavelengths in the non-absorbing visible and the moderately absorbing solar infrared part of the spectrum (Nakajima and King 1990; Han et al. 1994; Nakajima and Nakajima 1995; Watts et al. 1998).Scientific Updates since CPP version 3.9

The main updates in CPP v5.2 since v3.9 that was used for the generation of CLAAS Edition 1 are the following:

- Generation of new look-up tables (LUTs) based on DAK radiative transfer simulations. The most important changes in the LUTs are: extension of the range of solar zenith angles (SZAs) and viewing zenith angles (VZAs) using pseudospheric correction, and increase of the number and range of effective radii.
- Implementation of a new cloud typing algorithm, from which the cloud-top phase is derived. The new cloud typing algorithm closely follows the approach taken by the CLAVR-x team.
- Inclusion of observational sea ice and numerical weather prediction (NWP) snow cover data to better characterize the surface albedo.

4. Algorithm description

4.1. Theoretical description

The principle of the CPP retrieval algorithm is that the reflectance of clouds at a non-absorbing wavelength in the visible region (VIS: 0.6 or 0.8 μm) is strongly related to the optical thickness and has little dependence on particle size, whereas the reflectance of clouds at an absorbing wavelength in the near-infrared region (NIR: 1.6 or 3.8 μm) is primarily related to particle effective radius. This feature allows the retrieval of COT and REF from two channels of a passive imager. Moreover, Figure 1 shows that the imaginary parts of the refractive indices of water and ice, which are a measure for absorption, differ. For example, around 1.6 and 3.8 μm ice particles are more absorbing than water droplets. This feature, together with a series of spectral tests on the thermal infrared (IR) window channels is used to retrieve cloud-top thermodynamic phase.
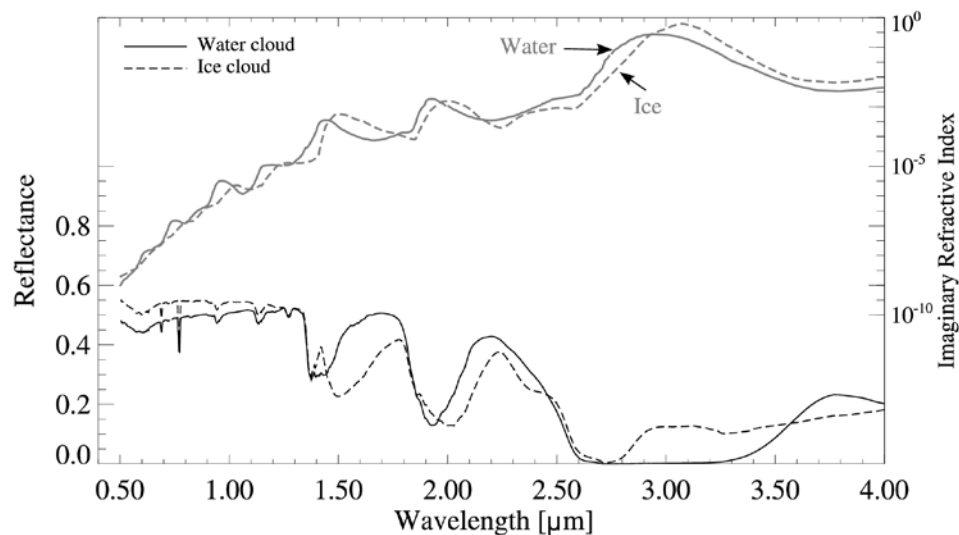
Figure 1: Simulated top-of-atmosphere (TOA) reflectance spectra for a stratocumulus (water) cloud and a cirrus (ice) cloud, and the imaginary part of the index of refraction of water and ice. The simulations were made with MODTRAN at $\theta_0 = 45°$, $\theta = 0°$ and $\varphi = 0°$. The reflectances are plotted as black lines, while the refractive indices are plotted as gray lines.

The cloud optical thickness is defined at 0.6 μm under the assumption of a plane parallel atmosphere with reference to a vertical transect. The particle effective radius r_e is the relevant quantity for radiative scattering, and is given by the ratio of the mean particle volume V to the mean projected cross-sectional area A (e.g., Schumann et al., 2011):

$$r_e = (3V)/(4A) \tag{1}$$

In case of a collection of spherical water droplets, this can be rewritten to:

$$r_e = \frac{\int_0^\infty r^3 n(r) dr}{\int_0^\infty r^2 n(r) dr} ,$$ (2)

where r is the droplet radius, and $n(r) dr$ is the number of particles per unit volume with radius between r and $r+dr$.

Liquid Water Path (LWP) is computed from the retrieved т and r_e by (Stephens 1978):

$$LWP = \frac{2}{3} \tau r_e \rho_l ,$$ (3)

where ρ_l = 1 g cm^{-3} is the density of water. Ice Water Path (IWP) is computed analogously, but using the density of ice, ρ_i = 0.93 g cm^{-3}.

More details on the actual retrieval will be given in later sections.

4.2. Radiative transfer

In this section the radiative transfer calculations required to derive the cloud products are described, both for the cloud type and for the cloud optical properties.

4.2.1. Infrared radiative transfer for cloud type

The cloud type/phase algorithm needs cloudy-sky radiance profiles and clear-sky brightness temperatures as input in order to evaluate the measured brightness temperatures in the infrared. It was chosen to rely on the RTTOV algorithm [RD-3] to calculate these quantities. The used RTTOV version (11.3) has been developed within the NWP SAF. The model calculates radiances for satellite infrared or microwave nadir scanning radiometers based on atmospheric profiles of temperature, variable gas concentrations, cloud and surface properties. It takes into account the water vapour absorption and can additionally take into account absorption from ozone, carbon dioxide, nitrous oxide, methane and carbon monoxide provided user profiles. The spectral range of the RTTOV v11 model in the visible/infrared is 0.4-20 microns with spectral models for a large number of supported platforms and sensors provided with the algorithm. All details on the radiative transfer algorithm and assumptions are provided in RD-3.

The input to the RTTOV calculations are taken from grib files from European Centre for Medium-Range Weather Forecasts (ECMWF) analyses and/or short-term forecasts (see Section 4.5.2) regridded to the SEVIRI longitude-latitude grid using the Climate Data Operators (CDO: https://code.zmaw.de/projects/cdo/wiki) tool set. The required parameters entail vertical profiles of temperature, pressure and humidity, 2-meter values (temperature, wind, and humidity), skin temperature, and surface pressure. To reduce the computational time the RTTOV calculations are performed for blocks of 16x16 SEVIRI pixels, once for the surface type as specified in the RTTOV package (including monthly mean emissivity at 0.1 degrees spatial resolution) and once for water. These coarse-resolution calculations are then combined with a high-resolution land-sea mask in order to properly take into account the large contrast between the surface emissivity of water and other surfaces. Finally the satellite angles are used to enable the correct calculation of atmospheric extinction and transmission effects.

The two outputs used for the cloud type calculation are:

- overcast radiance profiles: the level to space overcast radiance given by a black cloud for each level;
- clear-sky brightness temperatures: BT equivalent to clear-sky TOA radiance.

These quantities are needed for SEVIRI channels 5, 7, 9, 10, and 11 (see Table 4). The outputs are written to an intermediate hdf file which is subsequently read by the cloud type algorithm (Section 4.3.1).

4.2.2. VIS-IR radiative transfer for cloud optical properties

The CPP algorithm compares satellite observed reflectances at visible and near-infrared wavelengths to look-up tables (LUTs) of simulated reflectances for given cloud optical thicknesses, particle sizes and surface albedos for water and ice clouds (Watts et al. 1998; Jolivet and Feijt 2003). The Doubling Adding KNMI (DAK) radiative transfer model has been used to generate the LUTs of simulated cloud reflectances. DAK has been developed for line-by-line or monochromatic multiple scattering calculations at UV, visible and near infrared wavelengths in a horizontally homogeneous cloudy atmosphere using the doubling-adding method (De Haan et al. 1987; Stammes 2001). The clouds are assumed to be plane-parallel and embedded in a multi-layered Rayleigh scattering atmosphere. The particles of water clouds are assumed to be spherical droplets with effective radii between 3 and 34 μm and an effective variance of 0.15. For ice clouds, imperfect (or roughened), randomly oriented, hexagonal ice crystals in monodisperse size distributions with effective radii between 5 and 80 μm are assumed. Scattering properties were calculated with Mie theory for spherical droplets and with a raytracing code using the geometric optics approximation (Hess et al. 1998) for the hexagonal ice crystals. Knap et al. (2005) demonstrated that roughened hexagonal crystals give adequate simulations of total and polarized reflectances of ice clouds.
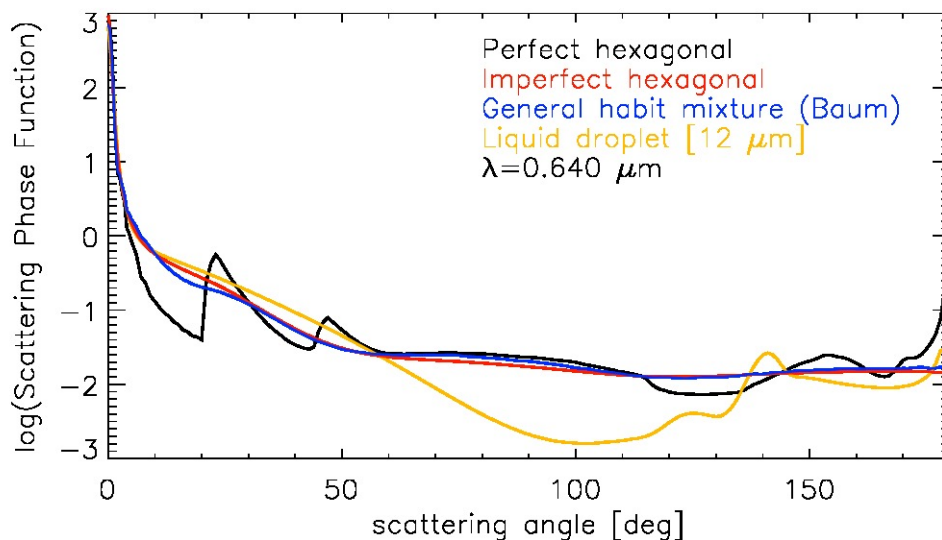
Figure 2: Comparison of scattering phase functions of water droplets, perfect (smooth) hexagonal ice crystals, imperfect (roughened) hexagonal ice crystals, and the Baum et al. (2011) roughened ice crystal habit mixture. The wavelength is 0.64 μm and the effective radii are 12 μm for the water droplets and 10 μm for the ice crystals.

Scattering phase functions of water droplets and ice crystals are compared in Figure 2. For water droplets a strong reduction in sideways scattering is observed as well as enhanced scattering at the rainbow angle and in backscatter direction. Smooth ice crystals tend to yield distinct halo features and a strong backscatter peak. In contrast, roughened crystals show virtually featureless phase functions, and also yield considerably lower asymmetry parameters compared to smooth crystals (Zhang et al., 2009). The recently revised phase functions for the official MODIS retrievals, based on a size distribution of a collection of roughened ice crystal shapes (Baum et al., 2011), are also plotted in Figure 2. They are remarkably similar to our phase functions, demonstrating that roughening has a far larger impact on phase functions than particle shape and size distribution.

Figure 3 shows an example of DAK calculations of 0.6 and 1.6/3.8 μm reflectances as function of τ and r_e for water droplets and ice crystals. The figure illustrates that for optically thick clouds lines of equal τ and particle size are nearly orthogonal, meaning that the 0.6 and 1.6/3.8 μm reflectances contain independent information on τ and r_e, respectively. This is not the case for optically thin clouds. Moreover, for these clouds, the lines of different r_e are very close together, implying that the retrieval of particle size is inherently more uncertain than for thick clouds. Further, it is evident that ice clouds have lower 1.6-μm and 3.8-μm reflectances than water clouds, which is a consequence of the stronger absorption of ice particles compared to water droplets at these wavelengths (see Figure 1). Although the features of the absorbing channels at 1.6 and 3.8 μm are similar, there are clear differences. At 3.8 μm the absorption by both water and ice is much stronger than at 1.6 μm. As a result, the dynamical range of reflectance is lower, but lines of equal τ and r_e are more orthogonal.
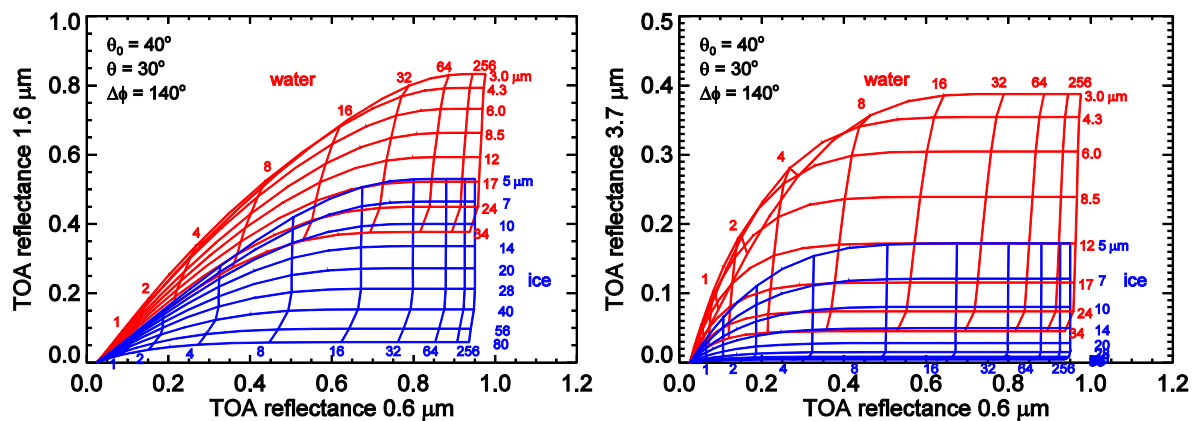
Figure 3: DAK calculations of TOA reflectance at 0.6 µm versus (a) 1.6 µm and (b) 3.8 µm for clouds consisting of spherical water droplets (red curves) and imperfect hexagonal ice columns (blue curves). The reflectances have been calculated over a black surface (albedo = 0). Solar and satellite angles are indicated in the plots. The vertically oriented lines represent lines of equal cloud optical thickness, while the horizontally oriented lines represent lines of equal particle size. Values of optical thickness and effective radius are indicated in the plot. Note the different scaling of the vertical axis in panels (a) and (b).

Table 2 summarizes the governing characteristics of the cloudy atmosphere, together with information about intervals of cloud properties and viewing geometries used in the DAK simulations to generate the LUT. The DAK simulations were done for a black surface. The TOA reflectance $R(\alpha_s)$ over a surface with reflectance α_s is computed using (Chandrasekhar, 1960):

$$R(\alpha_S) = R(\alpha_S = 0) + \frac{\alpha_s t_c(\theta_0) t_c(\theta)}{1 - \alpha_s \alpha_a} \qquad (4)$$

Here, $t_c(\theta_0)$ and $t_c(\theta)$ are the cloud transmissivities at the solar and viewing zenith angles, respectively, and α_a is the hemispherical sky albedo for upwelling, isotropic radiation. The required parameters are determined from two additional DAK calculations with surface reflectance values of 0.5 and 1.0.

Table 2: Properties of the cloudy atmosphere that are used for the radiative transfer calculations to generate the LUTs.

Parameter	Settings	
Vertical profiles of pressure, temperature, and ozone	Midlatitude summer [a]	
Aerosol model	None	
Cloud height	Water clouds: 1000-2000 m; Ice clouds: 5000-6000 m	
Solar zenith angle (θ_0) [b]	0 - 84.3° (73 Gaussian points in $\mu_0 = \cos(\theta_0)$)	
Viewing zenith angle (θ) [b]	Same as θ_0	
Relative azimuth angle (ϕ) [b]	0 - 180° (equidistant, 91 points)	
Cloud optical thickness	0 and 0.25 – 256, equidistant in log(τ) (22 points)	
	water clouds	**ice clouds**
Cloud particle type	Spherical water droplet	Imperfect hexagonal ice crystal [c]
Cloud particle size	3–34 μm equidistant in log(r_e), 8 points	5–80 μm equidistant in log(r_e), 9 points
Liquid / Ice water path	0 – 5,800 g m^{-2}	0 – 12,700 g m^{-2}
Size distribution	Two-parameter gamma	-
Effective variance (v_e)	0.15 [d]	-
Complex refractive index	Segelstein (1981)	Warren and Brandt (2008)

[a] The midlatitude summer atmosphere model was taken from Anderson et al. (1986).
[b] The chosen distributions of angles are motivated in Wolters et al. (2006).
[c] Aspect ratios of the imperfect hexagonal crystals are taken from Table 1 in Yang et al. (2013). To simulate the roughening a distortion angle of 30° is applied.
[d] This value is within the range found from in situ measurements. Different choices are possible, but the impact on the retrieved cloud properties is modest.

The DAK calculations concern monochromatic radiative transfer at a wavelength close to the centre of the respective satellite imager narrowbands. These calculations neglect scattering and absorption by atmospheric gases, except for Rayleigh scattering by air molecules and absorption by ozone. Before the reflectance simulated by DAK can be compared to an observed reflectance, the absorption by atmospheric gases in the band has to be taken into account. This so-called atmospheric correction has been implemented based on MODTRAN4.2 (Berk et al. 2000) radiative transfer simulations. The atmosphere-corrected TOA reflectance ($R_{atm.corr.}$) is calculated as:

$$R_{atm.corr.} = R \, t_{a,ac}(\theta_0, H_c, WVP) t_{a,ac}(\theta, H_c, WVP), \qquad (5)$$

where $t_{a,ac}$ is the above-cloud atmospheric transmissivity simulated by MODTRAN using a Lambertian surface placed at the cloud top height (H_c) and for a given water vapor path

(WVP). The two-way transmissivity, i.e. the product of the two transmissivities in Eq. (5), is a function of the geometrical air mass factor (AMF = $1/\mu_0 + 1/\mu$). This two-way transmissivity is stored in a LUT with dimensions AMF, H_c, and WVP. Absorption by trace gases within and below the cloud is neglected. An indication of the magnitude of the atmospheric correction is given in Table 3.

Table 3: Typical magnitude of atmospheric correction, expressed as 1 minus the two-way transmissivity, in %. The numbers have been calculated for a reference atmosphere (Hc = 2 km, AMF = 3, and WVP = 30 kg m-2), based on the MSG-SEVIRI spectral response, and for individual absorbing gases as well as for all gases together. Only the solar channels used for generating the CPP-SEVIRI data record, i.e. ch1 (0.6 μm) and ch3 (1.6 μm), are presented here.

Gas	Channel 1	Channel 3
H_2O	0.7 %	0.9 %
O_3	0.4 %	-
O_2	0.3 %	-
CO_2		2.7 %
CH_4		1.1 %
All gases	1.4 %	4.7 %

More details on the implementation of atmospheric correction and the effect on retrieved cloud properties can be found in Meirink et al. (2009).

4.3. Retrieval scheme

The CPP retrieval scheme consists of two parts. The first part is the retrieval of cloud type, and is described in Section 4.3.1. This cloud type is then reduced to two phases: liquid and ice. The second part is the retrieval of cloud optical properties (optical thickness and effective radius) for the retrieved phase. This is further described in Section 4.3.2.

4.3.1. Cloud type

The cloud type retrieval is based on a number of threshold tests using SEVIRI observed as well as clear- and cloudy-sky IR radiances and brightness temperatures. The algorithm is run for cloudy pixels and yields one of the following cloud types: liquid, supercooled, opaque ice, cirrus, overlap, and overshooting. The retrieval scheme follows developments by NOAA's CLAVR-x team. Here, we provide a complete overview of the spectral tests and the order in which they are performed.

In this section the wavelength λ refers to the SEVIRI channels 4 (solar-thermal IR, 3.9 μm), 5 (water vapour, 6.3 μm), 7 (window, 8.7 μm), 9 (window, 11 μm), 10 (window, 12 μm), and 11 (CO_2, 13 μm), see also Table 4.

First, a number of quantities, which are used in the algorithm, are introduced. The effective emissivity ε_λ expresses the observed radiance L_λ relative to the radiance $L_{\lambda,\mathrm{trop}}$ of a 'cold reference', being a black body at the tropopause height. It is defined by:

$$\varepsilon_\lambda = \frac{L_\lambda - L_{\lambda,clr}}{L_{\lambda,trop} - L_{\lambda,clr}}, \tag{6}$$

where $L_{\lambda,clr}$ is the clear-sky radiance. The beta parameter $\beta_{\lambda1-\lambda2}$ (e.g., Heidinger and Pavolonis, 2009) is a measure of cloud microphysics, and is defined by:

$$\beta_{\lambda_1 - \lambda_2} = \frac{\ln(1 - \varepsilon_{\lambda_2})}{\ln(1 - \varepsilon_{\lambda_1})}. \tag{7}$$

It is mainly used to detect the presence of liquid water below ice clouds. In the 3.9-μm channel both solar reflection and thermal emission contribute to the observed radiance. A reflectance ($R_{3.9}$) is defined by using T_{11} to obtain a blackbody radiance, assuming an emissivity of one at 11 μm, and a zero transmissivity at 3.9 μm (implying $R_{3.9} = 1 - \varepsilon_{3.9}$), leading to (e.g., Pavolonis et al., 2005):

$$R_{3.9} = \frac{L_{3.9} - B_{3.9}(T_{11})}{F_{0,3.9}\mu_0 - B_{3.9}(T_{11})}, \tag{8}$$

where $B_{3.9}(T_{11})$ is the Planck function at wavelength λ=3.9 μm applied to the brightness temperature at wavelength λ=11 μm, $F_{0,3.9}$ is the extraterrestrial solar flux in the 3.9-μm channel, and μ_0 the cosine of the solar zenith angle. Similarly, during nighttime, the emissivity is defined as:

$$\varepsilon_{3.9} = L_{3.9} / B_{3.9}(T_{11}), \tag{9}$$

The first step in the algorithm is the determination of an opaque cloud temperature T_c.

1. Using the water vapour channel
   This method is only applied if the following checks for high clouds are fulfilled:
   a. $L_{6.3,clr}$ - $L_{6.3}$ > 0.25,
   b. $L_{11,clr} - L_{11}$ > 2.0,
   c. $COV(T_{11}, T_{6.3})$ > 1.0, where COV denotes the covariance in the surrounding 5x5-pixel box.

A linear fit of the observed ($L_{11}, L_{6.3}$) against the simulated clear-sky ($L_{11}, L_{6.3}$) for the pixel under consideration is made. For a given layer, an overcast $L_{6.3}$ is then predicted applying the linear fit to the simulated overcast L_{11}. If this predicted overcast $L_{6.3}$ lies between the simulated overcast $L_{6.3}$ of the layer and the layer above, a match is found. T_c is set to the temperature of the lowest layer with such a match.

If no solution in this process is found or if the high-cloud checks are not fulfilled, indicating the cloud is low and opaque, the following method is used:

2. Using the 11-μm window channel
   The observed L_{11} is compared with the simulated profile of overcast L_{11}. The profile is scanned from troposphere to surface until two adjacent layers are found for which the observed radiance is between the respective simulated overcast radiances. T_c is found by interpolation between the temperature of these layers.

Based on T_c (in Kelvin) an ice phase probability p_{ice} is calculated as:

$$p_{ice} = MIN(1, MAX(0, 1 - (T_c - 243)/20)).$$

Subsequently, a series of empirical tests for water and ice clouds are performed.

1. The phase is set to water ($p_{ice} = 0$) if one of the following holds. The physical meaning of (a) and (b) is that liquid clouds are more reflective (less emissive) than ice clouds; (c) is based on a difference in relative absorption in the 8.7 and 11 µm channels between ice and water.
    a. Daytime ($\theta_0 \leq 84°$): $p_{ice} > 0$ and $R_{3.9} > 0.2$ and $\varepsilon_{s,3.9} > 0.9$, where ε_s denotes the surface emissivity
    b. Nighttime ($\theta_0 > 84°$): $p_{ice} > 0$ and $\varepsilon_{3.9} < 0.95$.
    c. $T_{8.7} - T_{11} < -1.0$.
2. The phase is set to ice ($p_{ice} = 1$) if the previous test did not yield water and one of the following cirrus tests is satisfied:
    a. $T_{11} - T_{12} - F_{WV} > 1.0$, where

$$F_{WV} = 0.5, \text{if } T_{11} \leq 265,$$

$$F_{WV} = (T_{11,clr} - T_{12,clr})\frac{T_{11} - 260}{T_{11,clr} - 260}, \text{if } T_{11} > 265.$$

    b. $COV(T_{11}, T_{6.3}) > 1.5$ and $MAX(T_{6.3}) < 250$, where MAX denotes the maximum in the surrounding 3x3-pixel box.

The cloud type is then determined as follows:

1. $p_{ice} \leq 0.5$
    a. $T_c < 273 \rightarrow$ supercooled
    b. $T_c \geq 273 \rightarrow$ water
2. $p_{ice} > 0.5$:
    a. $T_c < 233 \rightarrow$ opaque
    b. $T_c \geq 233$
        i. $\varepsilon_{11,tropo} < 0.8$
            1. $\beta_{11-12} < 0.95$ or $\beta_{11-13.4} < 0.7 \rightarrow$ overlap
            2. $\beta_{11-12} \geq 0.95$ and $\beta_{11-13.4} \geq 0.7 \rightarrow$ cirrus
        ii. $0.8 \leq \varepsilon_{11,tropo} \leq 0.95 \rightarrow$ opaque
        iii. $\varepsilon_{11,tropo} > 0.95 \rightarrow$ overshooting

The next step in the algorithm is a consistency check with the cloud-top temperature. Very cold clouds are not allowed to be liquid, and warm clouds are not allowed to be ice. Concretely, if the cloud type is water or supercooled and $T_c \leq 231$ K, the type is re-set to cirrus or opaque (if cloud optical thickness has been retrieved and is larger than 3). If the cloud type is opaque, cirrus or overlap, and $T_c \geq 265$ K, the type is re-set to water.

Finally, the type is reduced to a cloud-top phase product, by setting the categories water and supercooled to liquid and the categories opaque ice, cirrus and overlap to ice. This phase enters the optical properties retrieval. As explained in the next section, it is possible that the optical properties retrieval is inconsistent with the assigned phase. In that case, the phase is switched (from liquid to ice or vice versa) and the type is switched accordingly. With that last step, which is obviously only applied during daytime, the cloud-top phase product is ready.

4.3.2. Cloud optical properties

The cloud optical thickness and particle size are retrieved in an iterative manner for cloudy pixels during daytime ($\theta_0 < 84^o$). During the iteration the retrieval of τ at the 0.6-μm channel is used to update the retrieval of r_e at the 1.6-μm channel, and vice versa. This iteration process continues until the retrieved cloud optical properties converge to stable values. The interpolation between cloud optical properties in the LUTs is done with polynomial interpolation in τ and linear interpolation in $\log(r_e)$. As stated in Section 4.2, the retrieved particle size values are unreliable for optically thin clouds. Therefore for thin clouds the retrieved effective radius is adjusted towards an assumed climatologically averaged effective radius of 8 μm and 26 μm for water and ice clouds, respectively, values that are close to the ones used by Rossow and Schiffer (1999). The adjustment is performed for clouds with $\tau < 5$ using a smooth weighting function that gives an increasing weight to the climatologically averaged effective radius with decreasing cloud optical thickness.

4.4. Error budget estimates

The retrieval of cloud optical thickness and effective radius from 2-channel backscattered solar radiation is a simple but heavily underconstrained problem. As a result, many uncertainties are associated to this retrieval problem (see Stephens and Kummerow (2007) for a review). Here we attempt to describe some of the most important error sources: errors in radiative transfer modelling, instrument/calibration errors and errors in ancillary data. In Section 5, further sources of uncertainty related to violation of basic retrieval assumptions are discussed.

Errors in radiative transfer

To assess the potential error caused by uncertainties in radiative transfer modeling, Roebeling et al. (2005) compared four well-known RTMs that use different methods to solve the equation of radiative transfer. All these models are suited for simulating short-wave and narrow-band radiances in a cloudy atmosphere. However, the codes have originally been developed and optimized for different applications. The following methods for solving radiative transfer were compared:

- Monte Carlo method

The Monte Carlo model (Macke et al. 1999) is a forward scheme with a local estimate procedure for radiance calculations. It is a straightforward model that can be extended from one-dimensional to two- or three-dimensional calculations (Davis et al. 1985). Monte Carlo treats multiple scattering as a stochastic process. The phase function governs the probability of scattering in a specific direction. Photons are emitted by a source (e.g. the sun or a lidar device) and undergo scattering and absorption events inside a predefined three-dimensional cloudy atmosphere until: (i) the intensity of the photons falls below a certain threshold (due to absorption), (ii) the photons escape from the system. After each scattering event, the intensity of the photons that contribute to predefined sensor viewing angles is calculated (local estimate procedure).

- Doubling Adding method

This is the method used in the DAK model introduced in Section 4.2. DAK first calculates the reflection and transmission of an optically thin layer, in which no more than two scattering events may occur. Thanks to this restriction the radiative transfer equation can be solved analytically. Next, the reflection and transmission of two identical layers on top of each other can be obtained by computing successive reflections back and forth between the layers. This doubling procedure is continued until the actual optical thickness of the cloud is reached. The

cloud is embedded in a multilayer Rayleigh scattering atmosphere. The DAK model includes polarization.

- Discrete Ordinates method

In the MODerate spectral resolution atmospheric TRANsmittance and radiance code (MODTRAN), the multiple scattering calculations are based on the Discrete Ordinate (DISORT) method (Stamnes et al. 1988). The radiative transfer equation is solved for N discrete zenith angles to obtain N equations for N unknowns. These unknowns may be solved numerically. The MODTRAN single scattering radiances are computed separately from DISORT with inclusion of spherical geometry effects; the plane-parallel DISORT single scattering contributions are subtracted from the DISORT radiances for generation of the total radiance values. For the comparisons a beta version, MODTRAN4v2r0, was used, in which user-defined phase functions for cloud particles could be specified.

- Spherical Harmonics Discrete Ordinates method

The Spherical Harmonics Discrete Ordinate Method SHDOM (Evans 1998) has been developed for modelling radiative transfer in inhomogeneous three-dimensional media. SHDOM uses an iterative procedure to compute the source function of the radiative transfer equation on a grid of points in space. The angular part of the source function is represented by a spherical harmonics expansion mainly because the source function is computed more efficiently in this way than in DISORT. A discrete ordinate representation is used in the solution process. The number of iterations increases with increasing single scattering albedo and optical thickness.

The intercomparison study demonstrated that SHDOM and DAK are suitable models for the calculations of narrow-band cloud reflectances. For a clear atmosphere all models showed small absolute differences relative to the reference model (Monte Carlo), while for a cloudy atmosphere considerably larger absolute differences were observed. The causes for the latter differences are due to numerical noise or differences in the multiple scattering calculations. The implementation of a user-defined phase function in MODTRAN4v2r0 (beta release) was a large improvement, it was still the least accurate model for the simulation of cloud reflectances in this study. On average MODTRAN simulations deviated less than 3% from the reference model, but for individual viewing angles in the principal plane the deviations can increase to about 30%. It was suggested that the differences in MODTRAN reflectances cannot be fully explained by the method for multiple scattering calculations (DISORT). Part of the observed differences may be explained by different or incorrect model parameterizations. However, MODTRAN has been further improved since the study by Roebeling et al. (2005). The DAK and SHDOM calculations were similar to Monte Carlo, with mean differences smaller than 3%. However, for individual cases the differences were occasionally much larger. A noticeable finding was that the Monte Carlo has a 3% bias as compared to SHDOM and DAK. This bias may be explained by differences in the treatment of the forward peak of the scattering phase function. Especially for large particles with a strong forward peak this may cause significant differences in simulated reflectances. Beside these differences, Monte Carlo showed small non-systematic oscillations relative to SHDOM and DAK. These oscillations were largest for optically thick clouds ($\tau = 64$), for moderate particle sizes ($r_e = 10$ μm) and for large viewing zenith angles (75°). For these cases the number of multiple scattering events is large (up to 200) and the forward peak is strong, such that small differences in single scattering parameters can easily accumulate to large errors in the reflectances (±2%). Finally, the used version of SHDOM became unstable at certain optical thicknesses and effective radii. Comprehensive analysis showed that these instabilities occur at 0.63 and 1.61 μm wavelengths and that the problem disappeared again by choosing another optical thickness or effective radius.

Instrument errors

The solar channels of SEVIRI are not calibrated on-board. Vicarious calibration is performed by EUMETSAT using desert and ocean targets. Inter-comparisons of reflectances revealed differences between SEVIRI and MODIS (Meirink et al., 2013). Thus, it was decided to calibrate the SEVIRI solar channels towards MODIS (see RD-2). As a result, the estimated accuracy should be of the same order as for MODIS, and is estimated to be around 3%. The thermal channels are presumably in a better shape because they are calibrated on board using blackbodies.

Errors in the observed reflectance translate non-linearly into errors in retrieved cloud properties, since the relationship between reflectance and cloud properties is non-linear. The CPP algorithm includes an error estimate for this retrieval error. We start from the functional relationship $R_{V,N} = f(\tau, r_e)$, where $R_{V,N}$ is the reflectance in the VIS or NIR channel. Derivation of this relation leads to:

$$\Delta R_{V,N} = \left. \frac{\partial R_{V,N}}{\partial \tau} \right|_{r_e} \Delta \tau + \left. \frac{\partial R_{V,N}}{\partial r_e} \right|_{\tau} \Delta r_e, . \tag{10}$$

where Δ denotes an error. The partial derivatives with respect to τ (r_e) are at constant r_e (τ), respectively. Equation (10) can be inverted to:

$$\Delta \tau = \frac{1}{F} \left(\left. \frac{\partial R_N}{\partial r_e} \right|_{\tau} \Delta R_V - \left. \frac{\partial R_V}{\partial r_e} \right|_{\tau} \Delta R_N \right); \tag{11}$$

$$\Delta r_e = \frac{1}{F} \left(- \left. \frac{\partial R_N}{\partial \tau} \right|_{r_e} \Delta R_V + \left. \frac{\partial R_V}{\partial \tau} \right|_{r_e} \Delta R_N \right), . \tag{12}$$

with

$$. \; F = \left. \frac{\partial R_V}{\partial \tau} \right|_{r_e} \left. \frac{\partial R_N}{\partial r_e} \right|_{\tau} - \left. \frac{\partial R_V}{\partial r_e} \right|_{\tau} \left. \frac{\partial R_N}{\partial \tau} \right|_{r_e} . \tag{13}$$

The retrieval error in LWP follows directly from the errors in τ and r_e. These relations are applied in CPP with a 3% relative error in the VIS and NIR reflectance. The resulting error estimates relate to the propagation of reflectance errors into errors in retrieved cloud properties, and do not cover error sources discussed further on in this document.
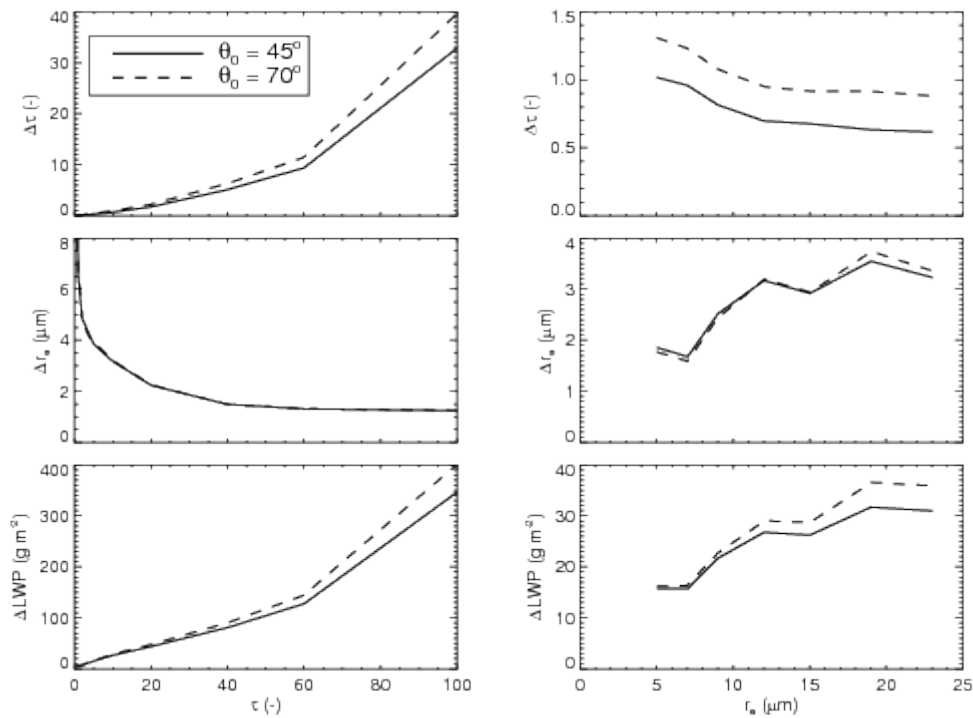
Figure 4 CPP retrieval errors as calculated using Eqns. (10) – (13). The errors in τ (top), r_e (middle), and LWP (bottom) are shown as a function of τ (left, with r_e = 12 μm kept constant) and r_e (right, with τ = 10 kept constant). The calculations were done for θ_0 = 45° and θ_0 = 70°, θ = 30° and φ = 90°, and are based on the 0.6-/1.6-μm channel combination.

Figure 4 shows the estimated retrieval errors for typical conditions, and their dependence on the cloud properties. Two important features are illustrated by this figure. First, the cloud optical thickness retrieval becomes highly uncertain for thick clouds as a result of the asymptotic relation between visible reflectance R and cloud optical thickness τ. The derivative $d\tau/dR$ increases with increasing τ, and for large values of τ a marginal change in visible reflectance causes a large increase in the retrieved cloud optical thickness. Second, the error in effective radius is generally between 2 and 3 μm, but becomes much larger for thin clouds. For this reason the retrieval of r_e for thin clouds is weighed towards a climatological value, as was discussed in Section 4.3. Figure 4 shows that errors get larger at high solar zenith angles, but not dramatically. Errors may increase more for particular parts of the phase function, e.g. the backward scattering peak or the rainbow.

Errors in ancillary data

A significant source of retrieval error is caused by uncertainties in surface reflectance α_s. This is illustrated in Figure 5, which displays the impact on retrieved LWP of a – realistic – 25% (relative) uncertainty in α_s. Deviations of α_s in the non-absorbing channel (left panels) mainly affect the retrieved cloud optical thickness. The impact is relatively largest for thin clouds because the TOA outgoing radiation over these clouds contains a considerable contribution from the surface. Deviations of α_s in the absorbing channel (right panels) mainly affect the retrieved effective radius. This impact is also largest for thin clouds, but due to the weighing with a climatological effective radius it is suppressed for the thinnest clouds. Hence, a maximum sensitivity is observed for an optical thickness around 5. In all cases LWP is more sensitive to uncertainties in α_s over the brighter land surfaces than over the darker ocean.

Over ice- and snow-covered surfaces, with a typical 0.6-μm surface albedo of 0.8, the retrieval becomes extremely sensitive, with LWP deviations of over 100% (not shown in Figure 5).
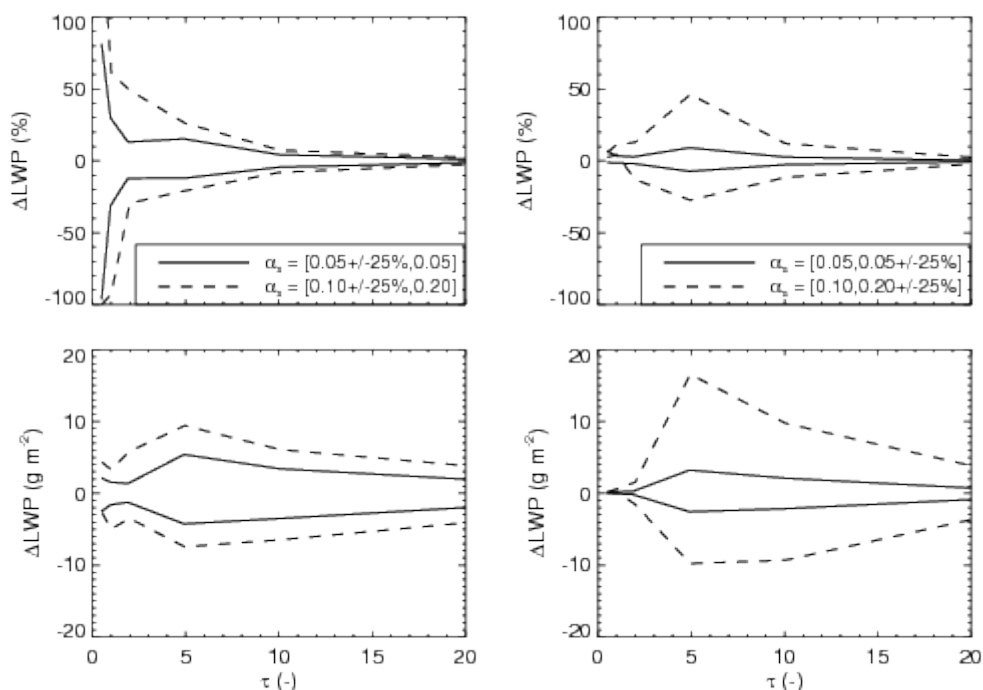
Figure 5: Sensitivity of retrieved LWP to uncertainties in surface reflectance. The curves show the relative (top panels) and absolute (bottom panels) deviation of LWP from the truth following from retrievals with a 25% increased or decreased surface reflectance in the 0.6-μm (left panels) and 1.6-μm (right panels) as a function of the true optical thickness. Two types of surfaces are distinguished: ocean with α_s = 0.05 at 0.6 and 1.6 μm (solid lines) and land with α_s = 0.1 at 0.6 and α_s = 0.2 at 1.6 μm (dashed lines). The calculations were done for θ_0 = 45°, θ = 30° and φ = 90°.

Another source of error is the ancillary data needed for the atmospheric correction. The largest impact is expected from uncertainties in the water vapour path and to a lesser extent the total ozone column. Errors in geolocation, solar angles and satellite angles can be assumed to be small, and hence their impact on cloud property retrievals is limited. Finally, the cloud mask, which is external input to the CPP algorithm (and thus considered here as ancillary data), is of importance. The cloud mask determines for which satellite pixels, a retrieval is performed. It does not influence the retrieval itself, i.e. the level-2 products, but it does have impact on aggregated level-3 products. Typically, a more selective cloud mask (i.e. assigning less pixels cloudy) leads to a larger aggregated cloudy-sky cloud optical thickness, because the thin/broken clouds will be excluded.

4.5. Practical Application

This section provides details on the SEVIRI instrument and other input data used by the CPP algorithm.

4.5.1. SEVIRI instrument

Meteosat Second Generation (MSG, Schmetz et al., 2002) is a series of European geostationary satellites that is operated by EUMETSAT. The first MSG satellite (METEOSAT-8) was launched successfully in August 2002, the second (METEOSAT-9) in December 2005, and the third (METEOSAT-10) in July 2012 The MSG is a spinning stabilized satellite that is positioned at an altitude of about 36,000 km above the equator and near 0° longitude. The SEVIRI instrument scans the complete disk of the Earth 4 times per hour, and operates 12 channels simultaneously. An overview of the spectral characteristics of the channels used by CPP is given in Table 4. The nominal spatial resolution of these channels is 3x3 km^2.

Table 4: SEVIRI channels used by CPP.

Channel	Channel name	Central wavelength (μm)	Nominal spectral band (μm)
1	*VIS006*	0.635	0.56 - 0.71
3	*IR_016*	1.64	1.50 - 1.78
4	*IR_039*	3.92	3.48 - 4.36
5	*WV_063*	6.25	5.35 - 7.15
7	*IR_087*	8.70	8.30 - 9.10
9	*IR_108*	10.80	9.80 - 11.80
10	*IR_120*	12.00	11.00 - 13.00
11	*IR_134*	13.40	12.40 - 14.40

4.5.2. Input data

In this section, the input data used to run the CPP algorithms are described.

Radiances

Radiances from the channels listed in Table 4 are the basic input.

Solar and satellite angles

The CPP algorithm requires the solar zenith angle θ_0, the satellite viewing zenith angle θ, and the relative sun-satellite azimuth angle ϕ. These angles are calculated by the CPP software itself.

Cloud mask

A cloud mask is needed to decide for which pixels a cloud physical properties retrieval will be attempted. The cloud mask of the NWC-SAF is used for this purpose (see RD-1). The CPP retrievals are run for pixels classified as *cloud contaminated* or *cloud filled*.

Cloud-top height and temperature

CPP uses the CTTH product from NWC-SAF (RD-1). For a fraction of the cloudy pixels, no cloud-top height/temperature retrievals are available. CPP then uses the spatially nearest retrieved values.

Surface albedo

Over land this is prescribed from a 5-year mean MODIS 0.6- and 1.6-µm snow-free gap-filled white-sky surface albedo database with 16-day resolution (Moody et al., 2004, 2008). This database was chosen because: (i) it is a frequently used and well recognized dataset; (ii) it contains the spectral channels needed for CPP SEVIRI processing; (iii) it has global extension and (iv) it is gap-filled. Over ocean the surface albedo is assumed to be 0.05 at both 0.6 µm and 1.6 µm.

Numerical Weather Prediction (NWP) model fields

The following NWP model fields are required:

- Vertical profiles of temperature, pressure and humidity; 2-meter values of temperature, wind, and humidity; skin temperature; surface pressure. These are needed for the clear-sky and overcast radiance calculations.

- Water vapour path. For the atmospheric correction the water vapour path is needed.

- Snow depth and snow albedo. These are used for the cloud type determination and to correct the MODIS snow-free albedo in case of snow on the ground. The snow parameters are not mandatory input, in the sense that the algorithm will still run if they are missing, but obviously with lower quality in snow-affected areas.

The NWP fields are obtained from operational ECMWF data or ERA-Interim (Dee et al., 2011).

Total ozone column

For the atmospheric correction the total ozone column is required. This is taken as a monthly mean climatology from the MSR dataset (Van der A et al., 2010).

Sea ice concentration

The concentration of sea ice is used for the cloud type determination and to correct the albedo of sea for the presence of ice. It is obtained from the Ocean and Sea-Ice (OSI) SAF. Like the snow parameters, this input is not mandatory.

4.5.3. Description of output

Here, the output fields in CPP level-2 files are listed with their name, data content and units. All products except cph and cph_ext are available only in daylight conditions ($\theta_0 < 84^o$).

cph   cloud-top thermodynamic phase, classes: liquid, ice

cph_ext   cloud-top thermodynamic phase, extended to more classes: water, super-cooled, opaque, cirrus, overlap, overshooting

cwp   cloud water path (LWP/IWP), unit: kg/m^2

cot   cloud optical thickness, dimensionless

reff   cloud particle effective radius, unit: m

dcwp   error estimate for cloud water path, unit: kg/m^2

dcot   error estimate for cloud optical thickness, relates to cpp_cot, dimensionless

dreff   error estimate for cloud particle effective radius, unit: m

qa   status flag, bit flag, described below (see Table 5)

hsigma   ratio of standard deviation of $R_{0.6}$ to mean $R_{0.6}$ over 3x3 pixels, dimensionless

Table 5: CPP status flag.

Bit number	Meaning
0	No optical properties retrieval performed
1	Cloud-free retrieved by optical properties retrieval
2	Phase changed by optical properties retrieval
3	VIS-NIR reflectance pair below solution space in LUT
4	VIS-NIR reflectance pair above solution space in LUT
5	Retrieval possibly affected by sunglint
6	Snow/ice at the surface according to auxiliary data
7	Negative NIR reflectance

5. Assumptions and Limitations

- In this section some of the assumptions and limitations associated with the retrieval algorithms are listed. The derivation of cloud physical properties from reflected solar radiation is dependent on the availability of daylight. This means that no retrievals can be done during night time. For cloud phase an IR-based algorithm is used, which does operate during nighttime as well as daytime.

- Sunglint can affect the cloud property retrievals considerably, in particular for broken cloudy scenes over ocean. Therefore, possibly sunglint-affected pixels (defined by a scattering angle differing less than 25 degrees from the direct glint angle) over ocean are flagged.

- Cloud retrievals are performed assuming that clouds are plane parallel. This is true only in a minority of cases, which implies that retrieval errors become larger as clouds deviate from being plane parallel. Especially convective clouds can be problematic, as they frequently have illuminated and shadowed sides (see, e.g., Marshak et al. 2006). Broken cloud fields can also cause problems for retrieving cloud properties, since a passive satellite sensor measures an averaged radiance of the cloudy and cloud-free part of a pixel. The error made in these cases is among others dependent on the contrast between clouds and underlying surface, the true properties of the cloud, and the cloud fraction within the sampling resolution of the instrument (Oreopoulos and Davies 1998; Coakley et al. 2005; Wolters et al. 2010). In this respect, the SEVIRI instrument, which has a nominal (sub-satellite) resolution of 3x3 km^2 and much coarser towards the edge of the disc, is more strongly affected by biases due to deviations from the plane parallel assumption than many polar orbiting imagers, which have typical resolutions of 1x1 km^2.

- The retrieval is highly problematic over very bright surfaces, particularly ice and snow, as the visible reflectance from clouds is similar to that from the surface.

- Unlike active satellite instruments, which can derive cloud profile information, retrievals from passive satellite instruments are limited by the fact that the obtained signal emanates from a weighted integration of the profile. Since near-infrared radiation is only penetrating into the cloud to a certain depth (due to absorption by cloud particles), the retrieved cloud phase and effective radius are representative for the upper part of the cloud (Platnick 2001). The penetration depth depends on the amount of absorption by cloud particles, which is increasing with wavelength. This means that the retrieved r_e depends on which NIR spectral channel is used (in our case 1.6 μm). Seethala and Horvath (2010) and Zhang and Platnick (2011) noted that the 3.8 μm r_e can be significantly smaller than the 1.6 or 2.2 μm r_e in non-raining Sc clouds, for which one would expect, in contrast, a steady increase in r_e from 1.6 through 2.2 to 3.8 micron. They suggested that drizzle and/or 3D inhomogeneity effects might be the cause. Zhang et al. (2012) further investigated the effects of drizzle and cloud horizontal inhomogeneity on MODIS r_e retrievals using LES models and synthetic retrievals and found that drizzle does not have a strong impact but inhomogeneity, the plane-parallel bias, does.

- In the derivation of Eq. (3) for LWP and IWP it is assumed that the cloud particle effective radius is representative for the total column. In reality this assumption is not assured. For example, liquid water clouds often obey adiabatic theory leading to a different form of Eq. (3), in which the factor 2/3 is replaced by 5/9, with r_e defined as the effective radius at the cloud top. However, radiation at 1.6 μm penetrates a significant depth into the cloud, so that the derived r_e is representative of a larger vertical extent as compared to retrievals using channels at 2.1 or 3.8 μm. Seethala (2011) showed that for marine stratocumulus clouds, LWP derived using the SEVIRI 1.6 μm channel and a factor 2/3 in Eq. (3) is

	Algorithm Theoretical Basis Document **SEVIRI Cloud Physical Products** **CLAAS Edition 2**	Doc. No.: SAF/CM/KNMI/ATBD/SEVIRI/CPP Issue: 2.2 Date: 10.06.2016

CM SAF
The EUMETSAT Network of Satellite Application Facilities
Climate Monitoring

comparable to LWP derived using the MODIS 2.1 μm channel and a factor 5/9 in Eq. (3). This suggests that automatic adiabatic correction is applied by using the 1.6 μm channel. Deviations from vertical homogeneity are also common for ice clouds. Thick ice clouds often have small ice crystals at the top, which are not representative of the full vertical extent. As a consequence, IWP can be underestimated in these cases. Results are even more questionable for multi layer cloud systems. Here the derived effective radius (uppermost cloud) may be totally unrelated to any cloud below. So the relation between r_e and LWP/IWP is not applicable here.

- Aerosols are not considered in the CPP retrieval. This assumption is usually justified because aerosols reside below or within the cloud and their optical thickness is small compared to that of the cloud. However, if the aerosols reside above the cloud and if they are sufficiently absorbing, they can significantly lower the visible reflectance. The effect on the retrievals depends on the channel combination used and on the aerosol properties (Haywood et al. 2004). Using the 1.6-μm channel, a possible understimation of r_e by several microns is possible. Cloud optical thickness generally has a low bias. Although the annual mean effect of absorbing aerosols is relatively small, their instantaneous effect on LWP can be as high as a 40 g m^{-2} low bias, mostly caused by a reduction in optical thickness. Wilcox et al. (2009) and Seethala and Horvath (2010) both have given estimates of absorbing aerosol effects on MODIS LWP by comparing it with passive microwave retrievals and quantifying the aerosol load with the help of OMI aerosol index. Seethala (2011) obtained similar estimates for SEVIRI LWP by comparison to TMI microwave retrievals.

- Precipitation may have an effect on cloud property retrievals in case the radiation penetrates sufficiently deep into the cloud to be affected by the (large) precipitating droplets. Retrievals with the 1.6-μm channel are expected to be most sensitive to this, but synthetic studies (e.g., Zinner et al. 2010; Zhang et al. 2012) have not indicated significant impact on the effective radius retrieval.

- Many assumptions are made for the calculation of LUTs with DAK. These include: the absence of aerosols, the specific habits and resulting phase functions of ice crystals, and the type and width of water droplet effective radius distributions. The necessity of these assumptions is an illustration of the heavily underconstrained nature of the cloud physical properties retrieval principle.

6. References

Ackerman, S.A., W.L. Smith, R.E. Revercomb, and J.D. Spinhirne, 1990: The 27–28 October 1986 FIRE IFO Cirrus Case Study: Spectral Properties of Cirrus Clouds in the 8–12 µm Window, *Mon. Wea. Rev.*, 118, 2377-2388.

Anderson, G. P., S. A. Clough, F. X. Kneizys, J. H. Chetwynd, and E. P Shettle, 1986: AFGL Atmospheric Constituent Profiles (0-120km). Tech. Rep. AFGL-TR-86-0110, 43 pp.

Baum, B. A., P. Yang, A. J. Heymsfield, C. G. Schmitt, Y. Xie, A. Bansemer, Y.-X. Hu, and Z. Zhang, 2011: Improvements in shortwave bulk scattering and absorption models for the remote sensing of ice clouds, *J. Appl. Meteorol. Clim.*, 50, 1037-1056, doi:10.1175/2010JAMC2608.1.

Berk, A., G. P. Anderson, P. K. Acharya, J. H. Chetwynd, L.S. Bernstein, E. P. Shettle, M. W. Matthew, and S. M. Adler-Golden, 2000: MODTRAN4 Version 2 Users Manual. Technical report, Air Force Materiel Command, Air Force Research Laboratory, Space Vehicles Directorate, Hanscom AFB, MA 01731, USA.

Chandrasekhar S., 1960: *Radiative Transfer*, New York, Dover, 393 pp.

Coakley, J. A., M. A. Friedman, and W. R. Tahnk, 2005: Retrieval of cloud properties for partly cloudy imager pixels, *J. Atmos. Ocean. Technol.,* 22 , 3–17.

Davis, J. M., T. B. McKee, and S. K. Cox, 1985: Application of the Monte Carlo method to problems in visibility using a local estimate: an investigation. *Appl. Optics*, 24, (19), 3193-3205.

De Haan, J. F., P. Bosma, and J. W. Hovenier, 1987: The adding method for multiple scattering calculations of polarized light, *Astron. Astrophys.*, 183, 371-391.

Dee, D. P., Uppala, S. M., Simmons, A. J., Berrisford, P., Poli, P., Kobayashi, S., Andrae, U., Balmaseda, M. A., Balsamo, G., Bauer, P., Bechtold, P., Beljaars, A. C. M., van de Berg, L., Bidlot, J., Bormann, N., Delsol, C., Dragani, R., Fuentes, M., Geer, A. J., Haimberger, L., Healy, S. B., Hersbach, H., Hólm, E. V., Isaksen, L., Kållberg, P., Köhler, M., Matricardi, M., McNally, A. P., Monge-Sanz, B. M., Morcrette, J.-J., Park, B.-K., Peubey, C., de Rosnay, P., Tavolato, C., Thépaut, J.-N. and Vitart, F., 2011: The ERA-Interim reanalysis: configuration and performance of the data assimilation system. Q.J.R. Meteorol. Soc., 137: 553–597. doi: 10.1002/qj.828

Evans, K. F., 1998: The Spherical Harmonics Discrete Ordinate, Method for Three-Dimensional Atmospheric Radiative Transfer. *J. Atmos. Sci.*, 55, 429-446.

Gao, B.-C. and W. J. Wiscombe, 1994: Surface-induced brightness temperature variations and their effects on detecting thin cirrus clouds using IR emission channels in the 8-12 micron region. *J. Appl. Met.*, 33, 568-570.

Greuell, W., E. van Meijgaard, J.F. Meirink, and N. Clerbaux, 2011: Evaluation of model predicted top-of-atmosphere radiation and cloud parameters over Africa with observations from GERB and SEVIRI, *J. Climate*, 25, 4015 – 4036, doi:10.1175/2011JCLI3856.1.

Greuell, W. and R. A. Roebeling, 2009: Towards a standard procedure for validation of satellite-derived Cloud Liquid Water Path: a study with SEVIRI data, *J. Appl. Meteorol. Clim.,* 48, 1575 – 1590, doi:10.1175/2009JAMC2112.1.

Han, Q., W. B. Rossow, and A. A. Lacis, 1994: Near-Global Survey of Effective Droplet Radii in Liquid Water Clouds Using ISCCP Data. *J. Climate,* 7, 465-497.

Haywood, J.M., S.R. Osborne, S.J. Abel, 2004: The effect of overlying absorbing aerosol layers on remote sensing retrievals of cloud effective radius and cloud optical depth, *Quart. J. Roy. Meteorol. Soc.*, 130, 779-800, doi: 10.1256/qj.03.100.

Heidinger A.K. and M.J. Pavolonis, 2009: Gazing at cirrus clouds for 25 years through a split window. Part I: Methodology, J. Appl. Meteorol. Clim., 48, 1100-1116, doi: 10.1175/2008JAMC1882.1.

Hess, H, R. B. A. Koelemeijer, and P. Stammes, 1998: Scattering matrices of imperfect hexagonal crystals. *J. Quant. Spectrosc. Radiat. Transfer*, 60, 301–308.

Jolivet, D., and A. J. Feijt, 2003: Cloud thermodynamic phase and particle size estimation using the 0.67 and 1.6 micron channels from meteorological satellites. *Atm. Chem. Phys. Discuss.*, 3, 4461-4488.

Knap, W. H., L. C. Labonnote, G. Brogniez, and P. Stammes, 2005: Modeling total and polarized reflectances of ice clouds: evaluation by means of POLDER and ATSR-2 measurements. *Appl. Optics*, 44, 4060-4073.

Macke, A., D. Mitchell, and L. von Bremen, 1999: Monte Carlo radiative transfer calculations for inhomogeneous mixed phase clouds. *Phys. Chem. Earth*, 24-3, 237-241.

Marshak, A., S. Platnick, T. Várnai, G. Wen, and R. F. Cahalan, 2006: Impact of three-dimensional radiative effects on satellite retrievals of cloud droplet sizes, *J. Geophys. Res.*, 111 , 9207–9218.

McFarquhar, G.M. and A.J. Heymsfield, 1998: The definition and significance of an effective radius for ice clouds, *J. Atmos. Sci.*, 55, 2039-2052.

Meirink, J.F., R.A. Roebeling, and P. Stammes, 2009: Atmospheric correction for the KNMI Cloud Physical Properties retrieval algorithm, KNMI publication: TR-304, 17/2/2009, pp22.

Meirink, J.F., R.A. Roebeling and P. Stammes, 2013: Inter-calibration of polar imager solar channels using SEVIRI, Atm. Meas. Tech., 6, 2495-2508, doi:10.5194/amt-6-2495-2013.

Minnis, P., K. N. Liou, and Y. Takano, 1993: Inference of Cirrus Cloud Properties Using Satellite-observed Visible and Infrared Radiances. Part I: Parameterization of Radiance Fields. *J. Atmos. Sci.*, 50, 1279–1304.

Moody, E. G., M. D. King, S. Platnick, C. B. Schaaf, F. Gao, 2004: Spatially complete global spectral surface albedos: Value-added datasets derived from Terra MODIS land products. *IEEE Trans. Geosci. Remote Sens.*, 43, 144-158.

Moody, E.G., M.D. King, C.B. Schaaf, and S. Platnick, 2008: MODIS-Derived Spatially Complete Surface Albedo Products: Spatial and Temporal Pixel Distribution and Zonal Averages. *J. Appl. Meteorol. Clim.*, 47, 2879–2894.

Nakajima, T., and M. D. King, 1990: Determination of the Optical Thickness and Effective Particle Radius of Clouds from Reflected Solar Radiation Measurements. Part 1: Theory. *J. Atmos. Sci .*, 47, 1878-1893.

Nakajima, T. Y., and T. Nakajima, 1995: Wide-Area Determination of Cloud Microphysical Properties from NOAA AVHRR Measurements for FIRE and ASTEX regions. *J. Atmos. Sci.,* 52, 4043 – 4059.

Oreopoulos, L., and R. Davies, 1998: Plane parallel albedo biases from satellite observations. part I: Dependence on resolution and other factors: *J. Climate*, 11 , 919–932.

Pavolonis, M. J., A. K. Heidinger, and T. Uttal, 2005: Daytime global cloud typing from AVHRR and VIIRS: Algorithm description, validation, and comparison, *J. Appl. Meteorol.*, 44, 804-826.

Platnick, S., 2001: A superposition technique for deriving mean photon scattering statistics in plane-parallel cloudy atmospheres, *J. Quant. Spectrosc. Radiat. Transfer*, 68, 57-73

Platnick, S., King, M. D., Ackerman, S. A., Menzel, W. P., Baum, B. A., Riedi, J. C., Frey, R. A., 2003: The MODIS cloud products: Algorithms and examples from Terra. *IEEE Trans. Geosci. Remote Sens.*, 41, 459-473.

Roebeling, R. A., 2008: Cloud Physical Properties Retrieval for Climate Studies using SEVIRI and AVHRR data, PhD Thesis, Wageningen University, The Netherlands, 160pp. Available from http://www.knmi.nl/publications.

Roebeling, R. A., A. Berk, A. J. Feijt, W. Frerichs, D. Jolivet, A. Macke, and P. Stammes, 2005: Sensitivity of cloud property retrievals to differences in narrow band radiative transfer simulations, KNMI Scientific Report, WR 2005-02, Royal Netherlands Meteorological Institute, De Bilt, the Netherlands, 27 pp. Available from http://www.knmi.nl/publications.

Roebeling, R. A., A. J. Feijt, and P. Stammes, 2006: Cloud property retrievals for climate monitoring: implications of differences between SEVIRI on METEOSAT-8 and AVHRR on NOAA-17, *J. Geophys. Res.*, 111, D20210, doi:10.1029/2005JD006990.

Roebeling, R.A., H. M. Deneke, and A. J. Feijt, 2008: Validation of cloud liquid water path retrieveals from SEVIRI using one year of CloudNET observations, *J. Appl. Meteorol. Clim.*, 47, 206-222.

Roebeling, R. A. and E. van Meijgaard, 2009: Evaluation of the Daylight Cycle of Model-Predicted Cloud Amount and Condensed Water Path over Europe with Observations from MSG SEVIRI, *J. Climate*, 22, 1749 – 1766, doi:10.1175/2008JCLI2391.1.

Rossow, W.B., and R.A. Schiffer, 1999: Advances in understanding clouds from ISCCP. *B. Am. Meteorol. Soc.*, 80, 2261-2287.

Schmetz, J., P. Pili, P., S. Tjemkes, D. Just, J. Kerkmann, S. Rota, A. Ratier, Alain, 2002: An Introduction to Meteosat Second Generation, Bull. Amer. Meteorol. Soc., 83, 7, 977-992.

Seemann, S.W., E. E. Borbas, R. O. Knuteson, G. R. Stephenson, H.-L. Huang, 2008: Development of a Global Infrared Land Surface Emissivity Database for Application to Clear Sky Sounding Retrievals from Multi-spectral Satellite Radiance Measurements, *J. Appl. Meteorol. Clim.*, 47, 108-123.

Seethala, C., 2011: Evaluating the diurnal cycle of clouds using CM-SAF SEVIRI VIS/NIR and TMI microwave retrievals, CM-SAF VS/AS19 report, 69pp. Available from http://www.cmsaf.eu.

Seethala, C. and A. Horvath, 2010: Global assessment of AMSR-E and MODIS cloud liquid water path retrievals in warm oceanic clouds, *J. Geophys. Res.*, 115, D13202, doi:10.1029/2009JD012662.

Segelstein, D., 1981: The complex refractive index of water, M.Sc. Thesis, Univ. of Missouri, Kansas City.

Schumann, U., B. Mayer, K. Gierens, S. Unterstrasser, P. Jessberger, A. Petzold, C. Voigt, J.-F. Gayet, 2011: Effective radius of ice particles in cirrus and contrails. *J. Atmos. Sci.*, 68, 300–321, doi:10.1175/2010JAS3562.1.

Stammes, P., 2001: Spectral radiance modeling in the UV-Visible range. IRS 2000: Current problems in Atmospheric Radiation, edited by W.L. Smith and Y.M. Timofeyev, pp 385-388, A. Deepak Publ., Hampton, Va.

Stamnes, K., S. C Tsay, W. Wiscombe, and K Jayaweera, 1988: Numerically stable algorithm for discrete ordinate method radiative transfer in multiple scattering and emitting layered media. *Appl. Optics,* 27, 2502-2509.

Stephens, G. L., 1978: Radiation profiles in extended water clouds: II. Parameterization schemes. *J. Atmos. Sci.*, 35, 2123-2132.

Stephens, G. L. and C. D. Kummerow, 2007: The Remote Sensing of Clouds and Precipitation from Space: A Review. *J. Atmos. Sci.*, 64 , 3742–3765.

Van der A, R. J., Allaart, M. A. F., and Eskes, H. J., 2010: Multi sensor reanalysis of total ozone, Atmos. Chem. Phys., 10, 11277–11294, doi:10.5194/acp-10-11277-2010.

Warren, S. G. and R. E. Brandt, 2008: Optical constants of ice from the ultraviolet to the microwave: A revised compilation*. J. Geophys. Res.*, 113, D14220, doi:10.1029/2007JD009744.

Watts, P. D., C. T. Mutlow, A. J. Baran, and A. M. Zavody, 1998: Study on Cloud Properties derived from Meteosat Second Generation Observations, Final Report, EUMETSAT ITT no. 97/181.

Wilcox, E. M., Harshvardhan, and S. Platnick, 2009: Estimate of the impact of absorbing aerosol over cloud on the MODIS retrievals of cloud optical thickness and effective radius using two independent retrievals of liquid water path, *J. Geophys. Res*., 114, D05210, doi:10.1029/2008JD010589.

Wolters, E. L .A., H. M. Deneke, B. J. J. M. van den Hurk, J. F. Meirink, and R. A. Roebeling, 2010: Broken and inhomogeneous cloud impact on satellite cloud particle effective radius and cloud-phase retrievals, *J. Geophys. Res.*, 115, doi:10.1029/2009JD012205.

Wolters, E. L. A., R.A. Roebeling, and A. J. Feijt, 2008: Evaluation of cloud-phase retrieval methods for SEVIRI onboard Meteosat-8 using ground-based lidar and cloud radar data, *J. Appl. Meteorol. Clim.*, 47, 1723-1738, doi:10.1175/2007JAMC1591.1.

Wolters, E. L. A., R. A. Roebeling, and P. Stammes, 2006: Cloud reflectance calculations using DAK: study on required integration points, KNMI Technical Report, TR-292, Royal Netherlands Meteorological Institute, De Bilt, The Netherlands, 17 pp. Available from http://www.knmi.nl/publications.

Yang, P., L. Bi, B. A. Baum, K.-N. Liou, G. W. Kattawar, M. I. Mishchenko, and B. Cole, 2013: Spectrally consistent scattering, absorption, and polarization properties of atmospheric ice crystals at wavelengths from 0.2 to 100 μm, *J. Atmos. Sci.*, 70, 330-347, doi:10.1175/JAS-D-12-039.1.

Zhang, Z., A. S. Ackerman, G. Feingold, S. Platnick, R. Pincus, and H. Xue, 2012: Effects of cloud horizontal inhomogeneity and drizzle on remote sensing of cloud droplet effective radius: Case studies based on large-eddy simulations, *J. Geophys. Res.,* 117, D19208, doi:10.1029/2012JD017655.

Zhang, Z., and S. Platnick, 2011: An assessment of differences between cloud effective particle radius retrievals for marine water clouds from three MODIS spectral bands, *J. Geophys. Res.*, 116, D20215, doi:10.1029/2011JD016216.

Zhang, Z., P. Yang, G. Kattawar, Riedi, J., Labonnote, L. C., Baum, B. A., Platnick, S., and Huang, H.-L., 2009: Influence of ice particle model on satellite ice cloud retrieval: lessons learned from MODIS and POLDER cloud product comparison, *Atmos. Chem. Phys.*, 9, 7115-7129, doi: 10.5194/acp-9-7115-2009.

Zinner, T., G. Wind, S. Platnick, and A.S. Ackerman, 2010: Testing remote sensing on artificial observations: impact of drizzle and 3-D cloud structure on effective radius retrievals, *Atmos. Chem. Phys.*, 10, 9535-9549, doi:10.5194/acp-10-9535-2010.

7. Glossary

Table 6: Explanation of abbreviations and acronyms included in this document.

Acronym / abbreviation	Definition
AMF	Air Mass Factor
AVHRR	Advanced Very High Resolution Radiometer
CLAVR-x	Clouds from AVHRR Extended
CM SAF	Climate Monitoring SAF
COT (or τ)	Cloud Optical Thickness
CPH	Cloud thermodynamic Phase
CPP	Cloud Physical Products
CTT/CTH	Cloud Top Temperature / Height
CWP	Cloud Water Path
DAK	Doubling Adding KNMI
DISORT	Discrete Ordinates
DWD	Deutscher Wetterdienst (German Met Service)
ECMWF	European Centre for Medium-Range Weather Forecasts
EUMETSAT	European Organisation for the Exploitation of Meteorological Satellites
IR	Infrared (wavelength range)
IWC	Ice Water Content
IWP	Ice Water Path
KNMI	Koninklijk Nederlands Meteorologisch Instituut (Dutch Met Service)
LUT	look-up-table
LWP	Liquid Water Path
MODIS	Moderate Resolution Imaging Spectroradiometer
MODTRAN	MODerate spectral resolution atmospheric TRANsmittance and radiance code
MSG	Meteosat Second Generation
NIR	Near-Infrared (wavelength range)
NOAA	National Oceanic and Atmospheric Administration
NWC SAF	Nowcasting and Very Short Range Forecasting SAF
NWP	Numerical Weather Prediction
OSI SAF	Ocean and Sea Ice SAF
REF (or r_e)	Effective radius

SAF	Satellite Application Facility
SEVIRI	Spinning Enhanced Visible and Infrared Imager
SHDOM	Spherical Harmonics Discrete Ordinates Method
TOA	Top Of Atmosphere
VIS	Visible (wavelength range)
WVP	Water Vapour Path

Table 7: Explanation of terms used in this document.

Term	**Meaning**
Brightness temperature	The temperature of a blackbody producing the same radiative flux as the observed flux in a given spectral band.
Cloud cover	Fraction of the sky obscured by clouds.
Cloud mask	Index specifying whether a satellite observed pixel is clear or cloudy, with possible additional categories such as 'cloud-contaminated'.
Cloud optical thickness	The optical thickness due to clouds. It is defined here at $0.6 \ \mu m$ with reference to a vertical path through the atmosphere.
Cloud-top height	Height above the surface of the upper boundary of a cloud.
Cloud-top temperature	Temperature at the upper boundary of a cloud.
Cloud water path	The total mass of cloud particles in a vertical column.
Effective radius	The ratio of the volume of (cloud) particles to their projected surface area.
Ice water path	The total mass of cloud ice particles in a vertical column.
Liquid water path	The total mass of cloud liquid particles (droplets) in a vertical column.
Optical thickness	Also: optical depth. The negative natural logarithm of the fraction of radiation at a particular wavelength that is not scattered or absorbed on a path.
Reflectance	The ratio of reflected radiation in a certain direction to incident radiation. It can relate to a particular wavelength as well as to a spectral band.
Surface albedo	The reflectance of a surface integrated over all zenith and azimuth angles. Black-sky surface albedo refers to a uni-directional incoming radiative flux, while white-sky surface albedo refers to diffuse incoming radiation.
Thermodynamic phase	The phase (liquid or ice) of cloud particles.